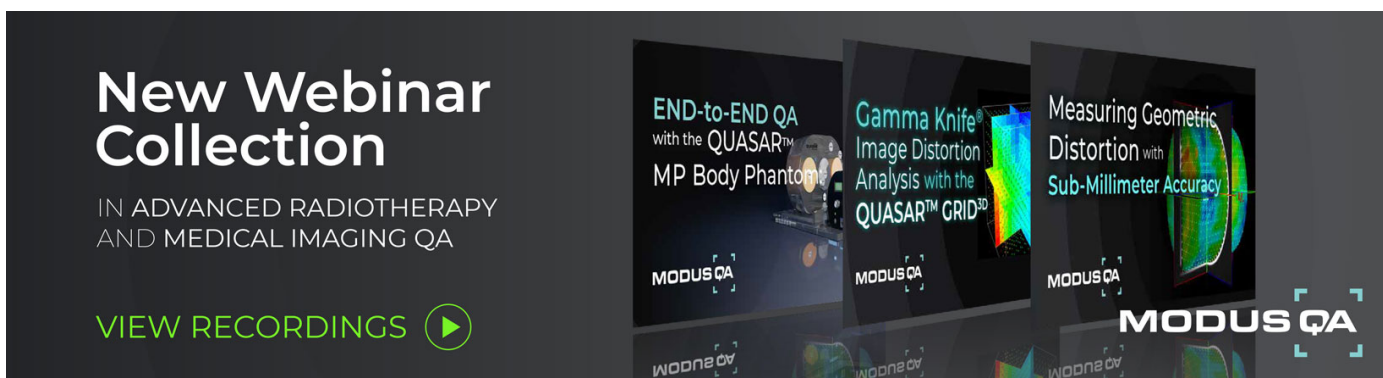


PAPER • OPEN ACCESS


## Simultaneous multi-slice accelerated 4D-MRI for radiotherapy guidance

To cite this article: K Keijne *et al* 2021 *Phys. Med. Biol.* **66** 095014

View the [article online](#) for updates and enhancements.



**New Webinar Collection**  
IN ADVANCED RADIOTHERAPY AND MEDICAL IMAGING QA

[VIEW RECORDINGS](#) 

**END-to-END QA with the QUASAR™ MP Body Phantom**

**Gamma Knife® Image Distortion Analysis with the QUASAR™ GRID<sup>3D</sup>**

**Measuring Geometric Distortion with Sub-Millimeter Accuracy**

**MODUS QA**



## PAPER


## Simultaneous multi-slice accelerated 4D-MRI for radiotherapy guidance

## OPEN ACCESS

RECEIVED  
8 January 2021REVISED  
10 March 2021ACCEPTED FOR PUBLICATION  
7 April 2021PUBLISHED  
28 April 2021

Original content from this work may be used under the terms of the [Creative Commons Attribution 4.0 licence](https://creativecommons.org/licenses/by/4.0/).

Any further distribution of this work must maintain attribution to the author(s) and the title of the work, journal citation and DOI.

K Keijne<sup>mans\*</sup> , P T S Borman , A L H M W van Lier, J J C Verhoeff , B W Raaymakers and M F Fast 

Department of Radiotherapy, University Medical Center Utrecht, Heidelberglaan 100, 3584 CX Utrecht, The Netherlands

\* Author to whom any correspondence should be addressed.

E-mail: [k.keijne@umcutrecht.nl](mailto:k.keijne@umcutrecht.nl)**Keywords:** 4D-MRI, simultaneous multi-slice, MR-linac, respiratory motion, mid-position, lung cancerSupplementary material for this article is available [online](#)**Abstract**

4D-MRI is becoming increasingly important for daily guidance of thoracic and abdominal radiotherapy. This study exploits the simultaneous multi-slice (SMS) technique to accelerate the acquisition of a balanced turbo field echo (bTFE) and a turbo spin echo (TSE) coronal 4D-MRI sequence performed on 1.5 T MRI scanners. SMS single-shot bTFE and TSE sequences were developed to acquire a stack of 52 coronal 2D images over 30 dynamics. Simultaneously excited slices were separated by half the field of view. Slices intersecting with the liver-lung interface were used as navigator slices. For each navigator slice location, an end-exhale dynamic was automatically identified, and used to derive the self-sorting signal by rigidly registering the remaining dynamics. Navigator slices were sorted into 10 amplitude bins, and the temporal relationship of simultaneously excited slices was used to generate sorted 4D-MRIs for 12 healthy volunteers. The self-sorting signal was validated using an *in vivo* peak-to-peak motion analysis. The smoothness of the liver-lung interface was quantified by comparing to sagittal cine images acquired directly after the SMS-4D-MRI sequence. To ensure compatibility with the MR-linac radiotherapy workflow, the 4D-MRIs were transformed into 3D mid-position (MidP) images using deformable image registration. Consistency of the deformable vector fields was quantified in terms of the distance discordance metric (DDM) in the body. The SMS-4D-TSE sequence was additionally acquired for 3 lung cancer patients to investigate tumor visibility. SMS-4D-MRI acquisition and processing took approximately 7 min. 4D-MRI reconstruction was possible for 26 out of 27 acquired datasets. Missing data in the sorted 4D-MRIs varied from 4%–26% for the volunteers and varied from 8%–24% for the patients. Peak-to-peak (SD) amplitudes analysis agreed within 1.8 (1.1) mm and 0.9 (0.4) mm between the sorted 4D-MRIs and the self-sorting signals of the volunteers and patients, respectively. Liver-lung interface smoothness was found to be in the range of 0.6–3.1 mm for volunteers. The percentage of DDM values smaller than 2 mm was in the range of 85%–89% and 86%–92% for the volunteers and patients, respectively. Lung tumors were clearly visible in the SMS-4D-TSE images and MidP images. Two fast SMS-accelerated 4D-MRI sequences were developed resulting in  $T_2/T_1$  or  $T_2$  weighted contrast. The SMS-4D-MRIs and derived 3D MidP-MRIs yielded anatomically plausible images and good tumor visibility. SMS-4D-MRI is therefore a strong candidate to be used for treatment simulation and daily guidance of thoracic and abdominal MR-guided radiotherapy.

**1. Introduction**

Respiratory motion is one of the main sources of targeting uncertainty for treatments in free-breathing external beam radiotherapy in the abdominal and thoracic regions (Keall *et al* 2006). Accurate tumor localization is of high importance to maximize the dose in the tumor and minimize the dose in organs at risk (OARs) and

surrounding healthy tissues. For organ motion management, respiratory phase resolved 4D imaging can be performed to capture tumor motion during the respiratory cycle. To date, 4D computed tomography (4D-CT) has been widely used to image patient-specific respiratory motion (Low *et al* 2003, Keall 2004).

In addition to 4D-CT, 4D magnetic resonance imaging (4D-MRI) is under active development for treatment MRI-simulation (MR-sim). Advantages of MRI over CT are: (1) superior soft-tissue contrast; (2) no radiation exposure during imaging; and (3) flexibility in selecting the imaging plane, as CT acquisition is limited to the transverse plane (Paganelli *et al* 2018, Stemkens *et al* 2018).

Recently, integrated MR-linac systems have been introduced, enabling online MRI-guided radiotherapy workflows (Olsen *et al* 2015, Raaymakers *et al* 2017). This gives the possibility to adapt the treatment daily to facilitate highly conformal radiation treatments. In the current clinical workflow of the Unity MR-linac (Elekta AB, Stockholm, Sweden), treatment plan adaptations can only be performed based on 3D-MRI. However, adapting based on 4D-MRI would be preferred since the radiation dose is delivered during free-breathing. Recently, Paulson *et al* (2020) have demonstrated a 3D-based 4D-MRI method that they incorporated in the online workflow of the Unity MR-linac. However, their method currently suffers from long reconstruction times (10 min).

4D-MRI acquisitions can be performed using multi-slice 2D or 3D imaging, which are retrospectively sorted into phase-resolved 3D volumes. Using 3D imaging, thinner slices can be acquired compared to 2D imaging. However, 2D imaging has the advantages of contrast flexibility and the fast image reconstruction time (i.e. in the order of seconds) (Paganelli *et al* 2018, Stemkens *et al* 2018). This fast reconstruction is made possible by utilizing the vendor provided reconstruction and standard DICOM creation before the data is sorted. Consequently, sorting is performed in the image domain by extracting an image domain self-sorting signal (Stemkens *et al* 2018).

2D-based self-navigation uses changes in body surface area or an internal anatomical structure visualized using MR images to extract a surrogate signal for respiratory sorting from the image information itself (von Siebenthal *et al* 2007, Cai *et al* 2011, Yang *et al* 2014, Celicanin *et al* 2015, van de Lindt *et al* 2018a, 2018b). Self-navigation using the superior soft-tissue contrast provides a physiologically plausible self-sorting signal suitable for amplitude binning. As a consequence, spatially consistent 4D-MRI reconstructions are obtained as opposed to more blurred reconstructions obtained using phase binning (Wink *et al* 2006), in which some phases summarize larger motion amplitudes than others. The liver-lung interface is most often used for abdominal and thoracic image based self-navigation. Since the main abdominal motion is in the craniocaudal (CC) direction, a sagittal or coronal slice orientation is often preferred for a self-navigation approach. Of the two, the coronal slice orientation is the most time-efficient orientation to cover the field of view (FOV) (van de Lindt *et al* 2018b).

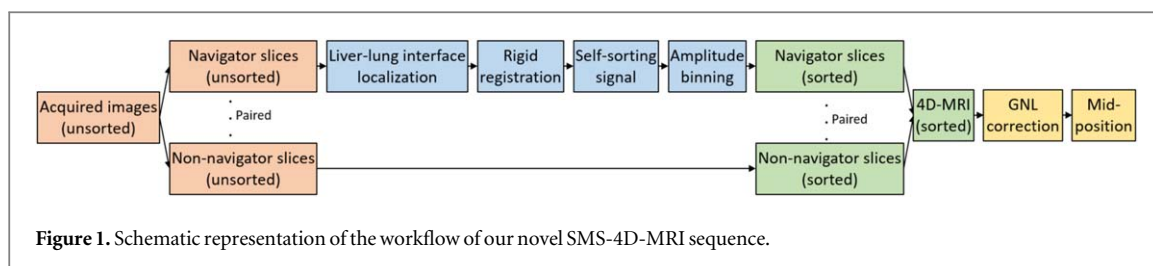
Conventional self-navigated multi-slice 4D-MRI acquisition results in a limited FOV in the through-plane direction, as the liver-lung interface has to be present in each slice location to be able to perform self-navigation. We hypothesize that the FOV limitation in 2D-based 4D-MRI can be overcome by using simultaneous multi-slice (SMS) imaging. In SMS imaging, multiple slices are acquired synchronously using a dedicated radiofrequency (RF) pulse, while the slices are disentangled in reconstruction using phase and/or coil encoding (Barth *et al* 2016). By acquiring multiple slices simultaneously while one of the slices, which is called the navigator slice, is always capturing the liver-lung interface, the FOV can be extended in the through-plane direction. The navigator slice is then used to retrospectively sort all simultaneously acquired slices into a 4D-MRI using image based self-navigation.

While 4D-MRI is best suited to characterize the complex dynamic nature of respiratory motion, the daily treatment adaptation workflow on the Unity MR-linac is not currently compatible with 4D imaging. To overcome this obstacle, 4D-MRI can be warped to a representative 3D mid-position (MidP) MRI. The MidP is the time-weighted average anatomy state, and typically does not coincide with a true respiratory phase from the 4D-MRI (van de Lindt *et al* 2019). It ensures the smallest possible planning target volume margins for treatment planning under free breathing conditions (Wolthaus *et al* 2008). By determining the MidP, a high resolution isotropic voxel-size can be achieved, overcoming the relatively coarse slice thickness of 2D imaging.

In this study, the first goal is to develop a fast SMS-4D-MRI free-breathing acquisition (~5 min) and post-processing (<2 min) method. The novel sequence should acquire full FOV thoracic and abdominal images on 1.5 T MRI scanners, and the post-processing should sort the 4D-MRIs and derive high resolution isotropic MidP images. The second goal is to demonstrate that the proposed SMS-4D-MRI method results in anatomically plausible patient representations with tumor visibility suitable for MRI-guided radiotherapy.

## 2. Methods and materials

Figure 1 shows a schematic representation of the workflow of our SMS-4D-MRI sequence. First, the SMS 2D data was acquired and reconstructed on the scanner, and then it was split into navigator and non-navigator



slices. Navigator slices were those slices that captured the liver-lung interface that were paired with non-navigator slices by synchronous acquisition. Second, the navigator slices were used for deriving the self-sorting signal and sorting the 4D-MRI. Third, gradient non-linearity (GNL) correction was applied, and lastly the MidP images were generated. Each processing step was performed in MATLAB R2019a (The MathWorks, Inc., Natick, USA). The following subsections explain each of the steps in more detail.

## 2.1. Acquisition SMS-4D-MRI

### 2.1.1. SMS-4D-MRI sequence design

In this study, two single-shot SMS coronal 4D-MRI sequences were developed: an SMS balanced turbo field echo (SMS-bTFE) sequence for  $T_2/T_1$  weighted contrast and an SMS turbo spin echo (SMS-TSE) sequence for  $T_2$  weighted contrast. An interleaved slice acquisition scheme was used to maximize the spatial distance between consecutive acquired slices and temporal distance between slices acquired at the same location, to prevent inter-slice cross-talk and slice saturation.

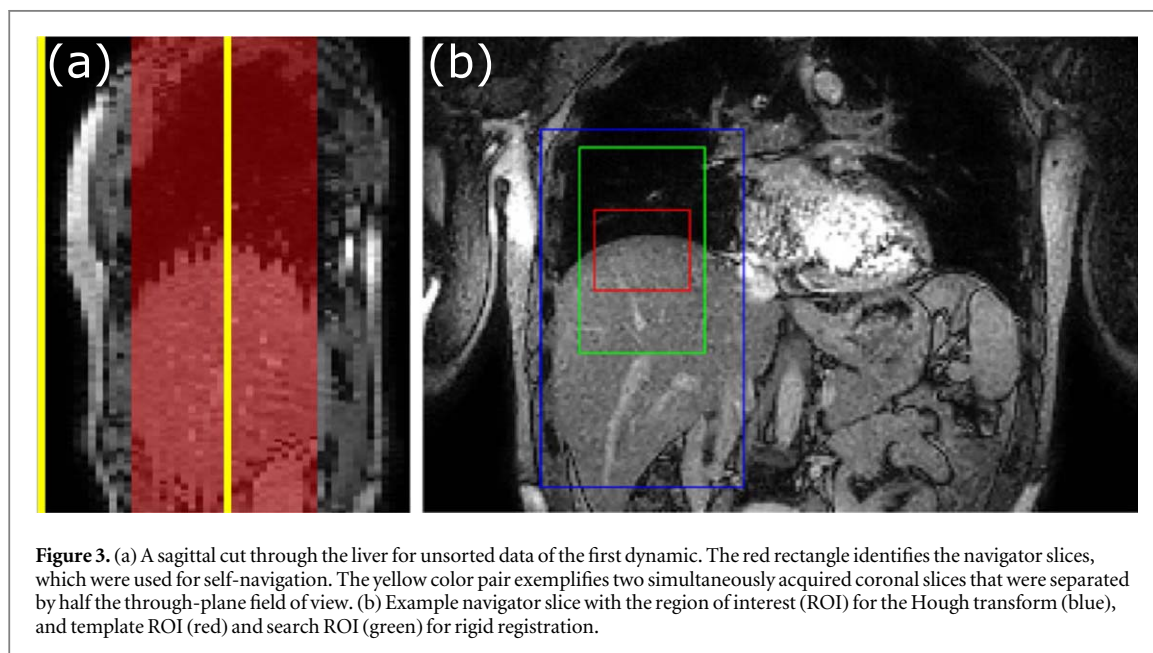
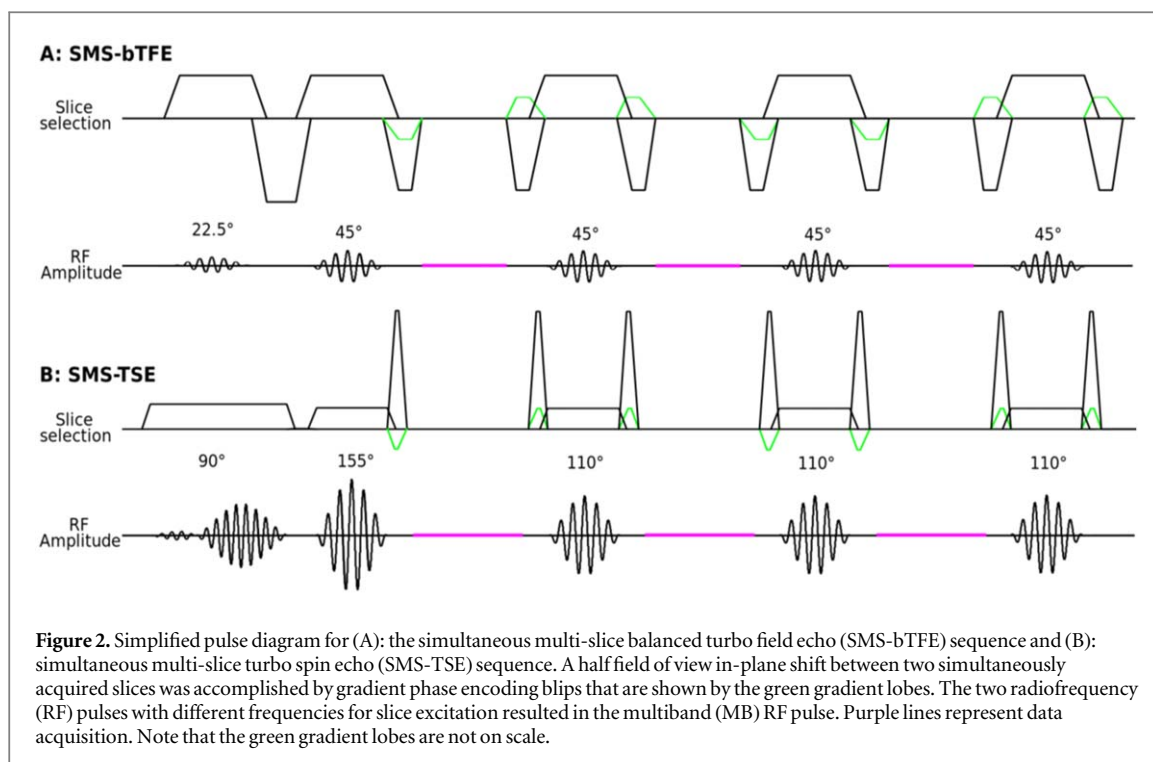
Two slices were acquired simultaneously that were separated by half the through-plane FOV, resulting in a better reconstruction performance due to the differences in coil sensitivity (Larkman *et al* 2001). Furthermore, controlled aliasing in parallel imaging results in higher acceleration (CAIPIRINHA) was implemented by applying phase cycling obtained by gradient phase encoding blips to get a half FOV in-plane shift of simultaneous acquired slices (Breuer *et al* 2006, Borman 2019). These two features have been implemented in the scanner software by extending the existing SMS functionality to make it compatible with the SMS-bTFE and SMS-TSE sequences. The two SMS slices were unfolded in the vendor provided reconstruction, which uses the SENSE algorithm (Pruessmann *et al* 1999, Larkman *et al* 2001). SENSE exploits the spatial coil sensitivity differences of the receive coil array to disentangle folded voxels correctly. Figure 2 shows a part of the SMS sequences containing the slice selection gradient and the multiband (MB) RF amplitude for both acquisition techniques.

### 2.1.2. SMS-4D-MRI data acquisition

**Healthy volunteers** The SMS-4D-MRI data consisted of 52 coronal slices acquired over 30 dynamics for all 12 healthy volunteers (age 22–39 years, weight 55–100 kg, male:female 11:1). The FOV was 300 (CC)  $\times$  450 left-right (LR)  $\times$  234–260 anterior-posterior (AP) mm<sup>3</sup>, and the voxel size was 2  $\times$  2  $\times$  4.5–5 mm<sup>3</sup>. The slice thickness was adapted to the anatomy of the volunteer. Directly after the SMS-4D-MRI scan, a 3 Hz sagittal cine scan was performed for 30 s. Further details can be found in the supplementary materials, available online at [stacks.iop.org/PMB/66/095014/mmedia](https://stacks.iop.org/PMB/66/095014/mmedia) (see scan parameters Unity MR-linac). The cine scan provided the anatomy of the liver-lung interface in the AP direction, that was used to quantify the performance of the 4D-MRI sorting method. Volunteer MRI examinations consisting of the SMS-4D-MRI sequences and the sagittal cine were performed on the Unity MR-linac. Written informed consent was obtained from all healthy volunteers.

**Patients** In this study, 3 lung cancer patients were scanned as part of their treatment MR-sim on a 1.5 T Ingenia MRI-scanner (Philips Healthcare, Best, The Netherlands). The SMS-TSE 4D-MRI scan was added to this exam, and consisted of 52 coronal slices acquired over 30 dynamics for all 3 patients (age 49–66 years, weight 61–112 kg, male:female 2:1). The FOV was 350 (CC)  $\times$  457 (LR)  $\times$  208–312 (AP) mm<sup>3</sup>, and the voxel size was 2  $\times$  2  $\times$  4–6 mm<sup>3</sup>. The slice thickness was adapted to the anatomy of the patient. Further details can be found in the supplementary materials (see scan parameters Philips Ingenia). Patient 1 had a cT1cN3M0 squamous cell lung carcinoma of the right upper lobe, patient 2 an rT0N0M1 invasive ductal breast carcinoma metastasis in a left hilar lymph node, and patient 3 an rT0N0M1 colon adenocarcinoma metastasis in the right perihilar region. Written informed consent was obtained from all patients.

Using the vendor provided optimal step-size for an interleaved acquisition, a total number of 52 slices was chosen to prevent saturation effects for the SMS-4D-MRI sequences. All SMS-4D-MRI images were acquired in free-breathing with arms down and without any vendor provided GNL correction.



## 2.2. Sorting 4D-MRI

### 2.2.1. Navigator slices

For sorting the 4D-MRI, the position of the liver-lung interface was used as a motion surrogate. Figure 3(a) shows that the middle half of the image stack intersects with the liver, and was therefore used as navigator slices. Moreover, this figure shows that the two simultaneously acquired slices were half an image stack apart from each other. As a result, the FOV in the through-plane direction was extended and images without the liver-lung interface were sorted correctly due to their temporal relationship with a simultaneously acquired navigator slice.

### 2.2.2. Liver–lung interface localization

The scans were performed in head-first supine position, which gave prior knowledge on the anatomy at the MR images. This prior knowledge was used to roughly crop out the right lung and liver in the coronal images, resulting in an image size of approximately 24 cm (CC)  $\times$  14 cm (LR). These reduced images were binarized using k-means clustering. Two clusters (roughly corresponding to liver and lung tissue) were used for the

SMS-bTFE acquired data. Three clusters (roughly corresponding to lung, liver, and fat tissue) were used for the SMS-TSE acquired data. After this, a circular object detection was performed using the circular Hough transform ( $4.5 \leq \text{radius} \leq 8.5$  cm) for localization of the liver-lung interface. For this approach, half of the navigator dataset (i.e. the odd dynamics) was used to determine the median liver-lung interface location for each slice location. This location was set as the midpoint of a template region of interest (ROI) with a length (CC) of 60 mm and a width (LR) of 50 mm that was used for the normalized cross-correlation. The ROIs can be found in figure 3(b).

### 2.2.3. Rigid registration

Acquired dynamics were rigidly registered to each other using normalized cross-correlation. An additional margin of 40 mm (CC) and 10 mm (LR) was added to the template ROI to set the search ROI for the normalized cross-correlation, see figure 3(b). As a result, cross-correlation was only applied to an area that was one-twentieth the size of the original images, reducing the computation time accordingly. With main abdominal motion being CC-motion, the displacement in CC direction between dynamics was determined. First, for each slice location all dynamics were registered to each other, i.e. each dynamic was used once as a reference. After outlier rejection, the most exhale dynamic was determined and used as the internal reference dynamic. Because end-exhale is the most stable respiratory phase, it was assumed that the end-exhale position was most stable across slice locations and did not suffer from motion artifacts and therefore had the best image quality to be used for the final image registration step. Second, a final normalized cross-correlation registration was performed using the selected reference dynamics, resulting in CC-shifts that had the end-exhale phase as reference. This final registration was performed using images up-sampled by a factor of 2 (i.e. 0.94 mm in-plane voxel size), to refine the registrations and therewith creating a less discretized self-sorting signal.

After the final registration step, the distribution of CC-shifts per slice location was evaluated. CC-shifts outside the range of (25th percentile  $-1 \times \text{IQR}$ , 75th percentile  $+1 \times \text{IQR}$ ) were marked as mis-registrations and corresponding slices were therefore not included in the 4D-MRI. Additionally, slice locations with a standard deviation (SD) of motion of less than half the voxel size were also excluded, as the registration results were assumed to be essentially noise. An additional correction was applied to the CC-shifts per slice location to correct for the non-uniform CC-motion of the liver across the AP direction as follows. The SD of CC-shifts per slice location was determined, and the maximal SD was chosen as reference. The CC-shifts per slice location were scaled with the ratio of their SD and the reference SD. This AP non-uniformity correction normalized the CC-motion of the liver-lung interface to a common reference location, and was first demonstrated by van de Lindt *et al* (2018b).

### 2.2.4. Self-sorting signal

By arranging the normalized CC-shifts in order of acquisition time, a self-sorting signal was derived that represented the CC-motion of the liver-lung interface at a reference slice location. Excluded registrations from the previous steps resulted in gaps in the self-sorting signal that were interpolated using a shape-preserving piecewise cubic spline interpolation. Gradient slopes between consecutive points in the self-sorting signal were determined to detect outliers. If the signs of three consecutive gradient slopes alternated, an outlier was detected and the corresponding data point was marked as an outlier. These rejected data points were also interpolated using a shape-preserving piecewise cubic spline interpolation.

### 2.2.5. Amplitude binning

Amplitude binning was performed on the previously derived self-sorting signal. An inclusion range of 95% of the data minimizing the peak-to-peak amplitude was used to effectively reject outlier motion (van Kesteren *et al* 2019). Moreover, the registrations that were detected as outliers in the previous two steps were excluded from the amplitude binning. Amplitude binning was chosen as it gives more spatially consistent 4D-MRI reconstructions compared to phase binning. However, it comes at a cost of missing data that has to be interpolated (van de Lindt *et al* 2018b). The data was binned into 10 respiratory phases describing one complete respiratory cycle consisting of inhalation and exhalation. By differentiating between inhalation and exhalation, hysteresis during breathing was taken into account. The end-exhale and end-inhale phases were halved in amplitude relative to the other phases to avoid oversampling. The centers of the amplitude bins were taken as reference point for the binning, i.e. the dynamic with the CC-shift closest to the bin center was used for the 4D-MRI if more dynamics were assigned to the same bin. Due to the temporal relationship between simultaneous acquired slices, the non-navigator slices were also sorted and therewith the full 4D-MRI was sorted. Missing data in the sorted 4D-MRI dataset was reconstructed using linear interpolation of neighboring slices and amplitude bins. Interpolation of missing slices was performed in an iterative fashion in case of clusters of missing data, starting with the missing slices with the largest amount of neighbors.

### 2.3. GNL correction

The current generation of MR scanners sacrifices linear gradients across the entire FOV for improvements in gradient switching speed and due to the shorter and wider bore designs, causing GNLs up to 1 cm over the FOV in all three principal directions. Therefore, GNL correction was applied to the sorted 4D-MRI dataset to obtain geometrically accurate images (Janke *et al* 2004, Keesman *et al* 2019).

### 2.4. Mid-position calculation

To ensure compatibility with the current Unity MR-linac radiotherapy workflow, MidP images were derived from the SMS-4D-MRI as planning images. The MidP was calculated by warping the 10 respiratory phases to their time-weighted average location using deformable vector fields (DVF) that were obtained using deformable image registration (DIR). The DVFs were obtained using the 'Adaptive (Auto)' module in ADMIRE (Advanced Medical Imaging Registration Engine) Research version 2.01 (Elekta AB, Stockholm, Sweden) and by EVolution with a regularization factor of 0.6 (de Senneville *et al* 2016). To determine the MidP images, the approach described by van de Lindt *et al* (2019) was used. First, all respiratory phases were non-rigidly registered to end-exhale. The average DVF of those registrations describes the DVF from the MidP to the end-exhale phase. Second, the end-exhale phase was registered to the other respiratory phases. Concatenating these two DVFs described the DVFs from the MidP to the individual respiratory phases. This approach can calculate the MidP images on a high resolution isotropic voxel grid, overcoming the coarse slice thickness of 2D-based 4D-MRI. Interpolated slices in the 4D-MRI were included in the DVF calculation. However, the resulting warped interpolated slices were excluded from the MidP calculation if not all respiratory phases of that particular slice location were interpolated. Otherwise, all interpolated slices were used for the MidP calculation to prevent missing data in the MidP images. Due to the study design of upsampling the data, a binary mask was determined describing the interpolated voxels, i.e. interpolated voxels had the value 1. All voxels that had a value  $>0.5$  after the interpolation step were excluded from the MidP calculation. For each voxel location in the MidP images, the weighted median was calculated using the weight distribution of the individual respiratory phases. These weights were obtained by tallying the number of contributing dynamics per 4D-MRI bin. In addition to the upsampled through-plane resolution, the orientation of the image-stack was altered to be axial, to ensure compatibility with the radiotherapy treatment planning workflows.

### 2.5. Validation

#### 2.5.1. Self-sorting signal

The most important component for the 4D-MRI sorting is the self-sorting signal, as it determines the binning of the data into the 4D-MRI dataset. The self-sorting signal was evaluated by a peak-to-peak analysis of the self-sorting signal itself and the sorted 4D-MRI datasets. For the self-sorting signal, the peak-to-peak amplitude was derived from the self-sorting signal normalized to the SD of the navigator slice that intersects the liver at its most cranial position. For the sorted 4D-MRI datasets, template matching between respiratory phases was performed. Due to the respiratory sorting approach of selecting the slice closest to the bin center, the peak-to-peak derived from the 4D-MRI was compared to 90% of the peak-to-peak amplitude of the self-sorting signal.

The AP non-uniformity correction of the CC-shifts per slice location, which was used to obtain the self-sorting signal, was validated using the cine images. By acquiring sagittal cine images directly after the scan, a ground truth depiction of the liver-lung interface in AP direction was acquired. An ROI was manually selected for the acquired cine images to only have the liver-lung interface present. Inside the ROI, the liver-lung interface was extracted using k-means clustering with three clusters. The extracted liver-lung interfaces were used to calculate the SD of CC-shifts for each voxel location on the liver-lung interface. Also, the SDs of CC-shifts of the navigator slices were interpolated to the cine image grid. Finally, both the calculated SD vectors of the CC-shifts were compared using the root-mean-square deviation (RMSD) metric.

Motion statistics from the self-sorting signals were extracted to characterize each respiratory pattern. The average (SD) peak-to-peak motion, average (SD) MidP location (relative to end-exhale), and average (SD) respiratory period were analyzed. All respiratory characteristics were correlated with the liver-lung interface smoothness using the Spearman's Rho non-parametric test.

#### 2.5.2. Liver-lung interface smoothness

To evaluate the temporal consistency of the sorted 4D-MRI volumes, the liver-lung interface smoothness was evaluated in the healthy volunteer datasets. As coronal 2D slices were acquired in this study, a sagittal cut through the sorted 4D-MRI was used to evaluate the through-plane liver-lung interface smoothness. The sorted 4D-MRI data acquired at the same spatial location as the cine image was extracted for the analysis. Afterwards, the liver-lung interface was extracted in both the subsequently acquired sagittal cine images and the sagittal cut through the 4D-MRI. For this, k-means clustering in a manually selected ROI was used as previously described.

For each separate respiratory phase, the liver-lung interface of the 4D-MRI was compared rigidly (translation only) to all liver–lung interfaces of the cine images, using an iterative closest point algorithm. As a metric, the RMSD was used. The cine point cloud that resulted in the smallest RMSD was chosen to quantify the liver-lung interface smoothness of the sorted 4D-MRIs and the MidP images.

### 2.5.3. Deformable vector fields

The MidP images were generated using DVFs obtained by DIR. To check their validity, the distance discordance metric (DDM) was used that quantified the performance of the DIR. The DDM calculation was based on the refined method proposed by van de Lindt *et al* (2019), which had modified the method of Saleh *et al* (2014). In our work, the method of van de Lindt *et al* (2019) was further refined. First, 3D DVFs from the end-exhale phase to the end-inhale phase were determined via the eight in between phases, resulting in eight 3D DVF maps pointing from each end-exhale voxel grid location to the corresponding end-inhale location. Second, DVFs from the individual phases to the end-exhale phase were determined, which were averaged and therefore described the DVF from the MidP to the end-exhale phase. As a result, the eight DVF maps (defined on the end-exhale phase) could be projected onto the MidP anatomy. For each voxel location, the SD of those eight points was used as DDM. The DDM values were evaluated within the body contour to quantify the reliability of the MidP images. A comparison was made between the distributions of DDM values obtained with ADMIRE and EVolution, and between DDM values smaller than 2 mm compared to the total DDM value distribution. The 2 mm cut-off was chosen, as the registration accuracy is typically desired to be within 2 mm for clinical applications (Brock *et al* 2017).

## 3. Results

Image acquisition on the Unity system took 5:17 and 4:56 min for the SMS-bTFE and SMS-TSE sequences respectively, and it took 4:44 min for the SMS-TSE sequence on the MR-sim. The average (SD) data processing time was 120 (2) s using ADMIRE and 78 (2) s using EVolution. Sorting and correcting the 4D-MRI took 32 s and generating the MidP took 16 s using an Intel Xeon W-2133 6-core CPU. Calculation of the DVFs for the MidP took 72 s using ADMIRE with a NVidia Tesla K20c GPU, and took 30 s using EVolution with a NVidia Titan V GPU.

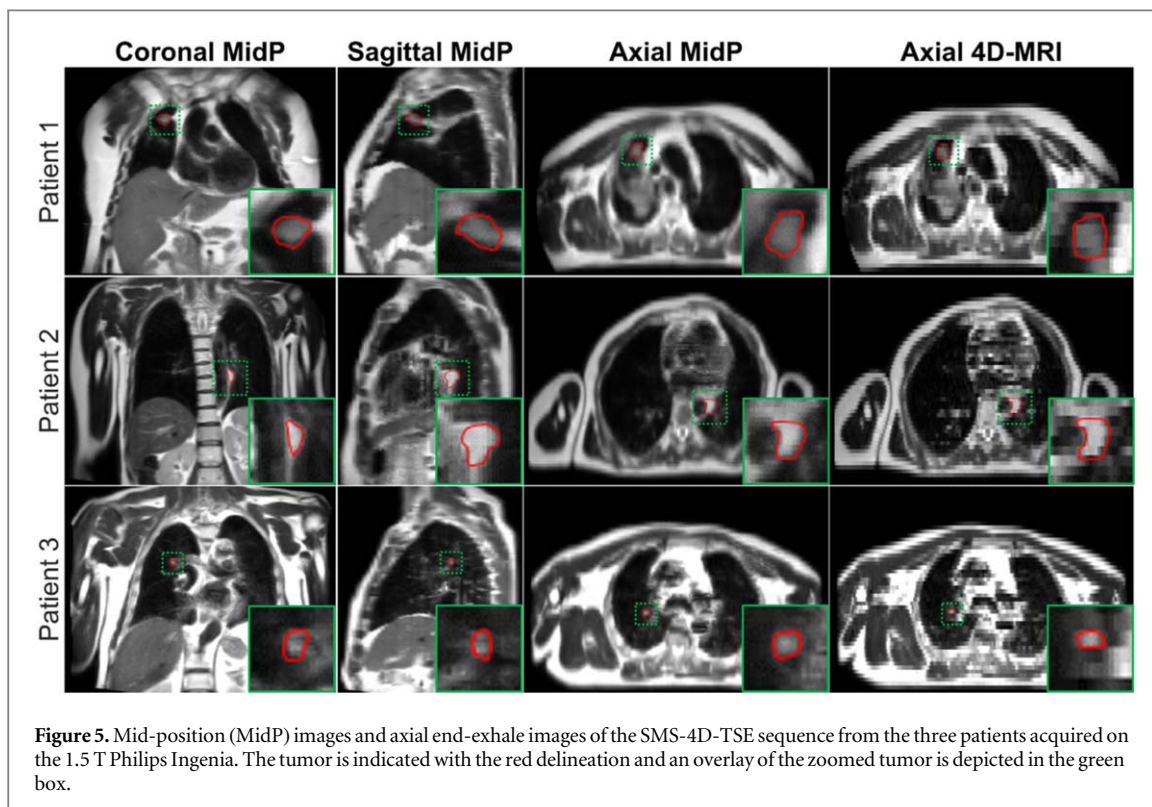
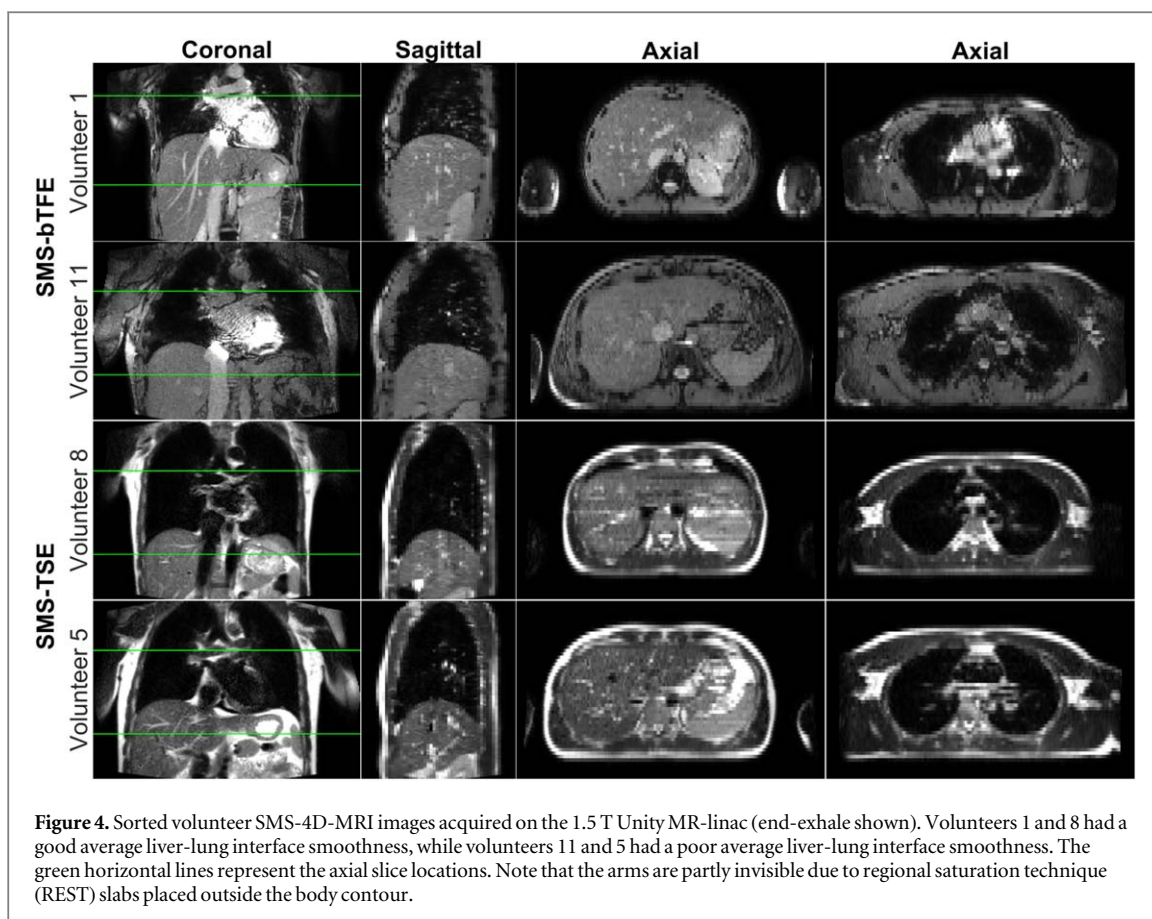
### 3.1. Image quality

All volunteer and patient SMS-4D-MRIs provided good visibility of abdominal organs, the lungs, and vessels based on visual assessment (figures 4 and 5). Additionally, good tumor visibility was achieved in the acquired patient datasets. However, small mediastinal structures, such as the esophagus and aorta, were less clearly visualized due to the relatively coarse slice thickness. The images acquired with both sequences on the Unity system appear noisier compared to the MR-sim. For the SMS-bTFE images, a black-boundary artifact occurred at water-fat interfaces and some cardiac motion induced artifacts were found in slices that contained the heart. For both acquisition techniques on the Unity system, a crescent-shaped SENSE artifact occurred for all volunteers that was most pronounced in the SMS-TSE acquired data. On the MR-sim this artifact only appeared in patient 1. For both acquisition systems, an additional artifact occurred in the SMS-TSE sequence at the liver that resulted in fluctuating signal intensity. This was randomly distributed over slice locations and dynamics, and the severity differed between volunteers and patients. These slices did not appear in the MidP images. The MidP images had less artifacts and noise, and more contrast compared to the individual respiratory phases.

### 3.2. Sorting 4D-MRI

4D sorting was possible for 23 out of 24 acquired image datasets of the volunteers, and was possible for all three acquired patient datasets. For the SMS-TSE image dataset of volunteer 11, the crescent-shaped SENSE image artifact appeared on the liver-lung interface, which hampered the rigid image registration and therefore the 4D-MRI sorting. Consequently, this dataset was excluded from further analysis. Figure 4 shows examples of SMS-4D-MRI images of healthy volunteers for the end-exhale phase, which were selected based on a good or a poor average liver-lung interface smoothness. Note that even in the case of relatively poor overall smoothness of the liver-lung interface, the end-exhale images look sharp in the sagittal view. The average (min–max) amount of missing data in the sorted SMS-4D-MRIs of the volunteers was 12.8% (5.8%–25.8%) for the bTFE sequence, and 13.0% (4.2%–23.5%) for the TSE sequence. For the patients the amount of missing data was in the range of 8.1%–23.8%.

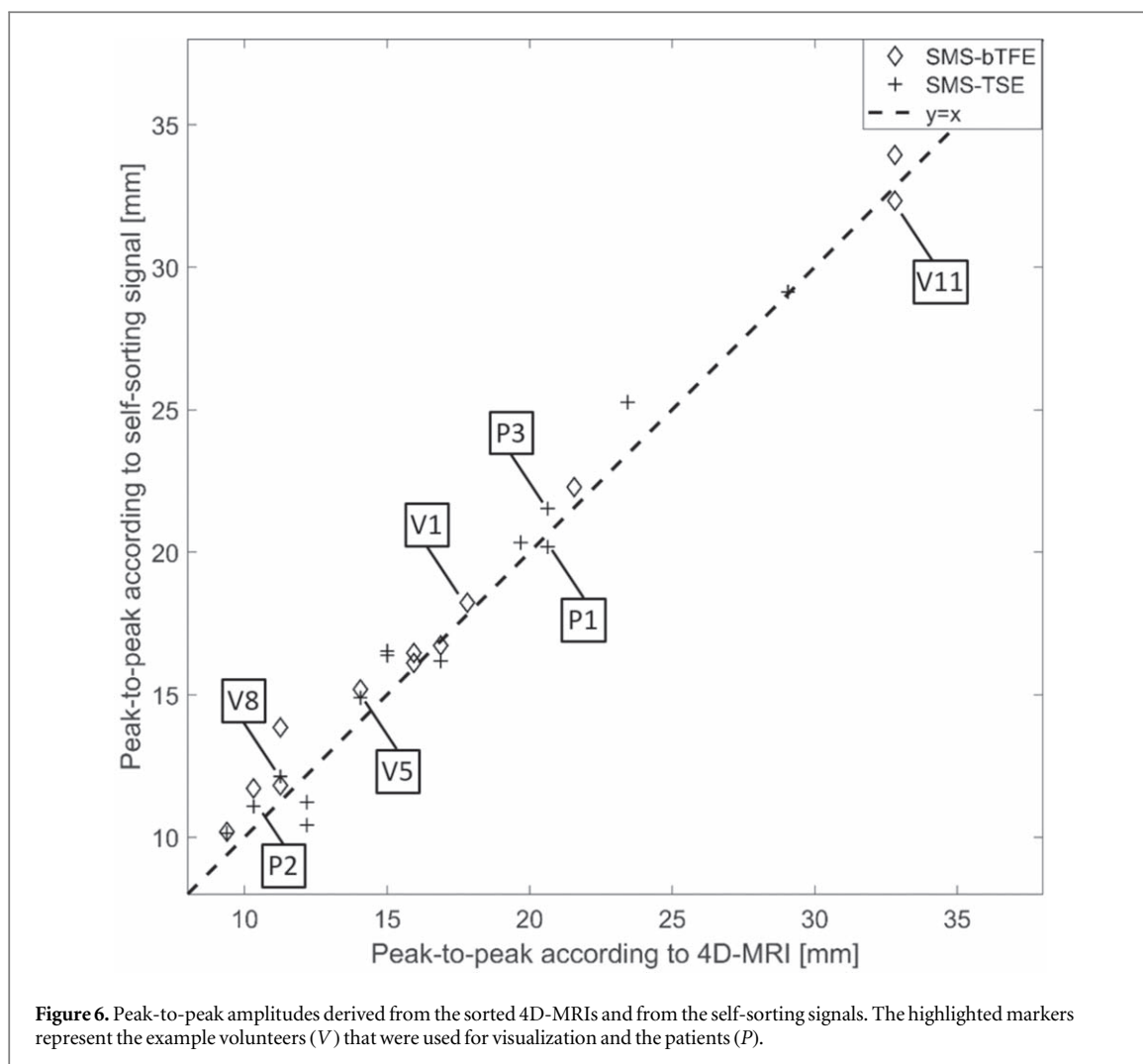




### 3.3. Validation

#### 3.3.1. Self-sorting signal

For the SMS-bTFE sequence, the peak-to-peak (weighted SD) motion in the sorted 4D-MRIs of the volunteers was between 9.4 and 32.8 (3.1–12.1) mm. Motion extracted from the corresponding self-sorting signals agreed



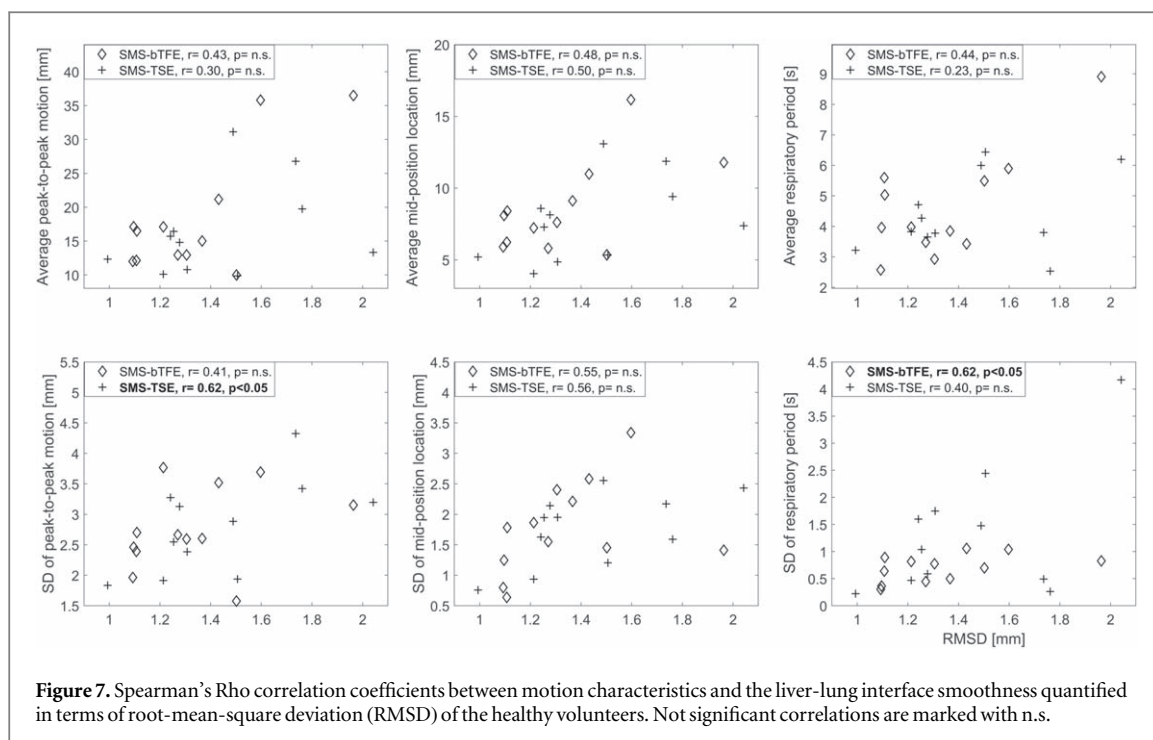
within 1.7 (0.9) mm. For the SMS-TSE sequence, the peak-to-peak (weighted SD) motion in the sorted 4D-MRIs of the volunteers was between 9.4 and 29.1 (3.2–10.8) mm. Motion extracted from the corresponding self-sorting signals agreed within 1.8 (1.1) mm. Peak-to-peak (weighted SD) motion in the sorted 4D-MRIs of the patients was in the range of 10.3–20.6 (3.3–5.9) mm, which was agreed within 0.9 (0.4) mm by the corresponding self-sorting signals. A two-sided Wilcoxon signed rank test was performed with a 5% significance level. All differences between peak-to-peak amplitudes and weighted SDs extracted from the 4D-MRIs and the self-sorting signals were found to be nonsignificant. All peak-to-peak amplitudes can be found in figure 6.

The average (min–max) RMSD between the SDs that were used for the AP non-uniformity correction of the CC-shifts and the SDs extracted from the sagittal cine images was 1.0 (0.4–2.0) mm. Results per volunteer can be found in the supplementary materials (see self-sorting signal: validation of AP non-uniformity correction).

Figure 7 shows the range of average (SD) peak-to-peak motion, average (SD) MidP location (relative to end-exhale), and average (SD) respiratory period of the healthy volunteers versus the liver-lung interface smoothness. The average (SD) peak-to-peak motion was in the range of 9.9–36.5 (1.6–4.3) mm, the average (SD) MidP location in the range of 4.0–16.2 (0.6–3.3) mm, and the average (SD) respiratory period duration in the range of 2.5–8.9 (0.2–4.2) s. For the SMS-bTFE 4D-MRI reconstructions, a moderate correlation was found for the SD of respiratory period versus the liver-lung interface smoothness. A moderate correlation was also found for the SD of peak-to-peak amplitude versus the liver-lung interface smoothness for the SMS-TSE 4D-MRI reconstructions. For the patients, the average (SD) peak-to-peak motion was in the range of 11.7–20.5 (1.5–6.9) mm, the average (SD) MidP location in the range of 5.4–11.6 (1.1–3.5) mm, and the average (SD) respiratory period in the range of 4.8–7.1 (0.9–4.0) s.

### 3.3.2. Liver–lung interface smoothness

The average (min–max) RMSD between the liver-lung interface extracted from the (volunteer) SMS-4D-MRI and sagittal cine was 1.3 mm (0.6–2.8 mm) for the SMS-bTFE sequence and 1.5 mm (0.8–3.1 mm) for the

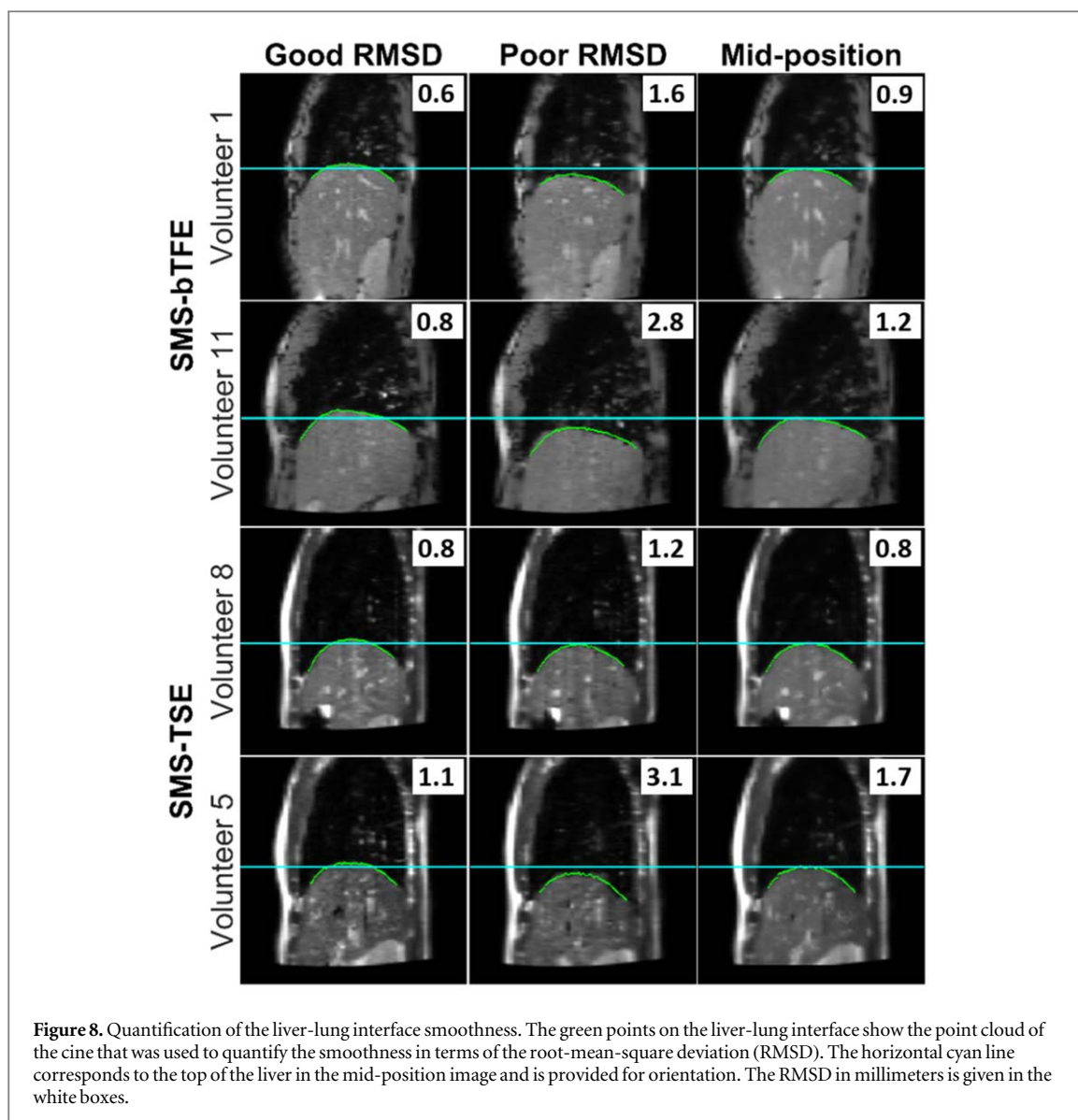


SMS-TSE sequence. The RMSD values of the MidP images were found to be in the range of 0.8–1.5 mm for the SMS-bTFE data and in the range of 0.8–1.8 mm for the SMS-TSE data. Similar or even better liver-lung interface smoothness was found for the MidP images compared to the average liver-lung interface over the respiratory phases, except for volunteer 3. The range of RMSD values for the sorted 4D-MRIs and MidP images can be found in the supplementary materials (see liver-lung interface smoothness). Figure 8 shows the sagittal cut-through of the SMS-4D-MRI at the same spatial location as the acquired sagittal cine image, with the cine-derived liver-lung interface providing the ground truth. This figure shows examples of respiratory phases with good (i.e. low RMSD value) and bad (i.e. high RMSD value) liver-lung interface smoothness, and the liver-lung interface smoothness of the MidP image. Better liver-lung interface smoothness was found at respiratory phases near end-exhale, while worse liver-lung interface smoothness was found at respiratory phases near end-inhale.

### 3.3.3. Deformable vector fields

The DDM within the body contour was determined for ADMIRE and EVolution. The histogram of DDM values can be found in figure 9. For the SMS-bTFE sequence, average (min–max) DDM values of 1.1 (0.0–15.2) mm and 1.0 (0.0–20.6) mm were found using ADMIRE and EVolution, respectively. For the SMS-TSE sequence, average (min–max) DDM values of 1.1 (0.0–15.7) mm and 0.8 (0.0–8.6) mm were found for ADMIRE and EVolution, respectively. For the patient datasets, average (min–max) DDM values of 1.0 (0.0–11.1) mm and 0.8 (0.0–15.8) mm were found for ADMIRE and EVolution, respectively. Using ADMIRE, 85.5% of the DDM values were smaller than 2 mm, and using EVolution, 87.0% of the DDM values were smaller than 2 mm for the SMS-bTFE dataset. For the SMS-TSE dataset, the percentages were 85.1% and 89.0% for ADMIRE and EVolution, respectively. For the patient datasets, the percentages were 86.2% and 91.5% for ADMIRE and EVolution, respectively.

Figure 10 shows examples of the spatial distribution of DDM values  $\geq 2$  mm that can be found locally on the MidP images obtained with EVolution. Regions of large DDM values can be found in the lungs, in the heart, in the skin, and in the epigastric region. This was at the expected locations, as cardiac and gastric motion were not taken into account during image acquisition. Furthermore, large DDM values in the skin were caused either by breathing or by banding artifacts arising from the SMS-bTFE sequence. Large DDM values in the lungs were found at locations of pulmonary arteries, which had different intensities for different respiratory phases caused by the pulsatile blood flow. Volunteers that had a poor liver-lung interface smoothness (i.e. high RMSD value) were found to have a lower registration accuracy (i.e. high DDM value).

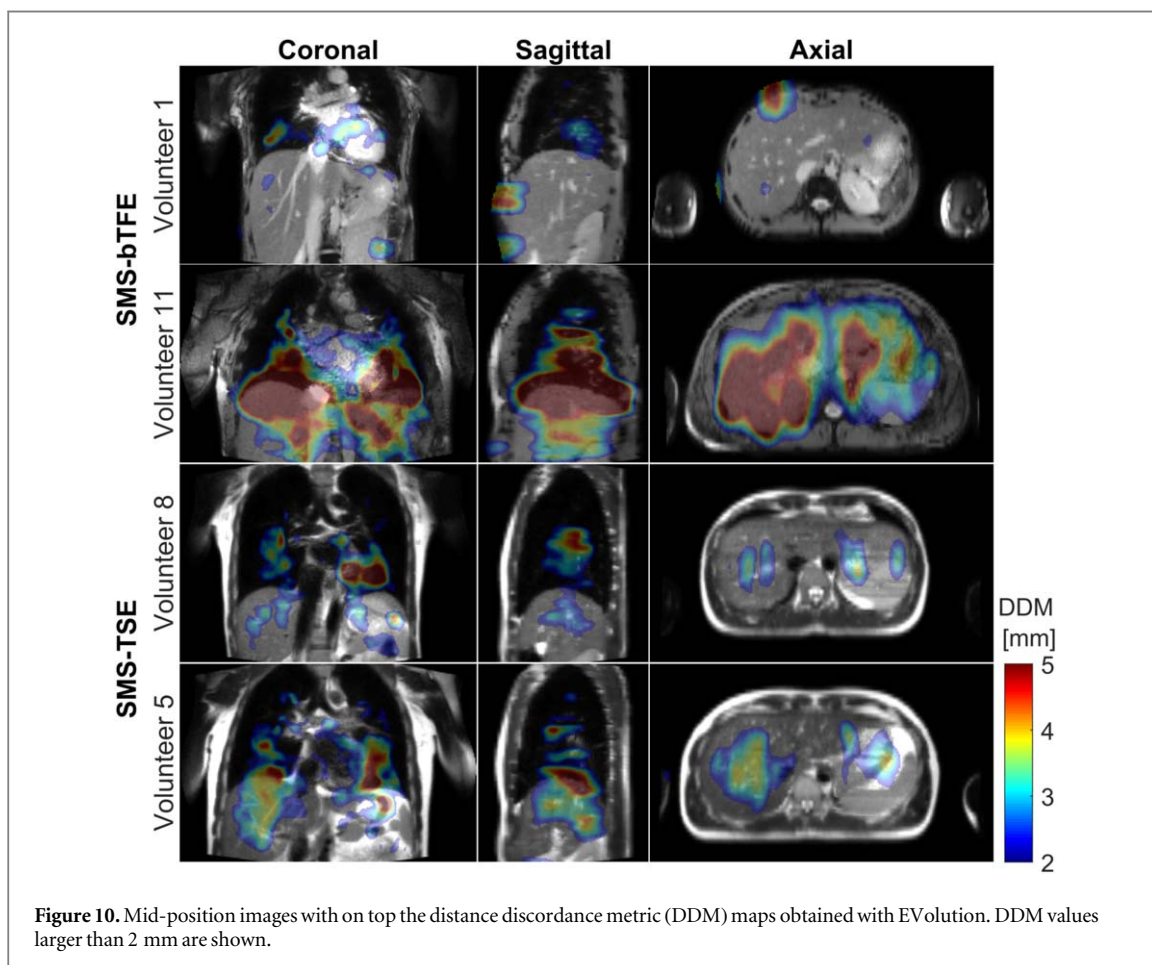
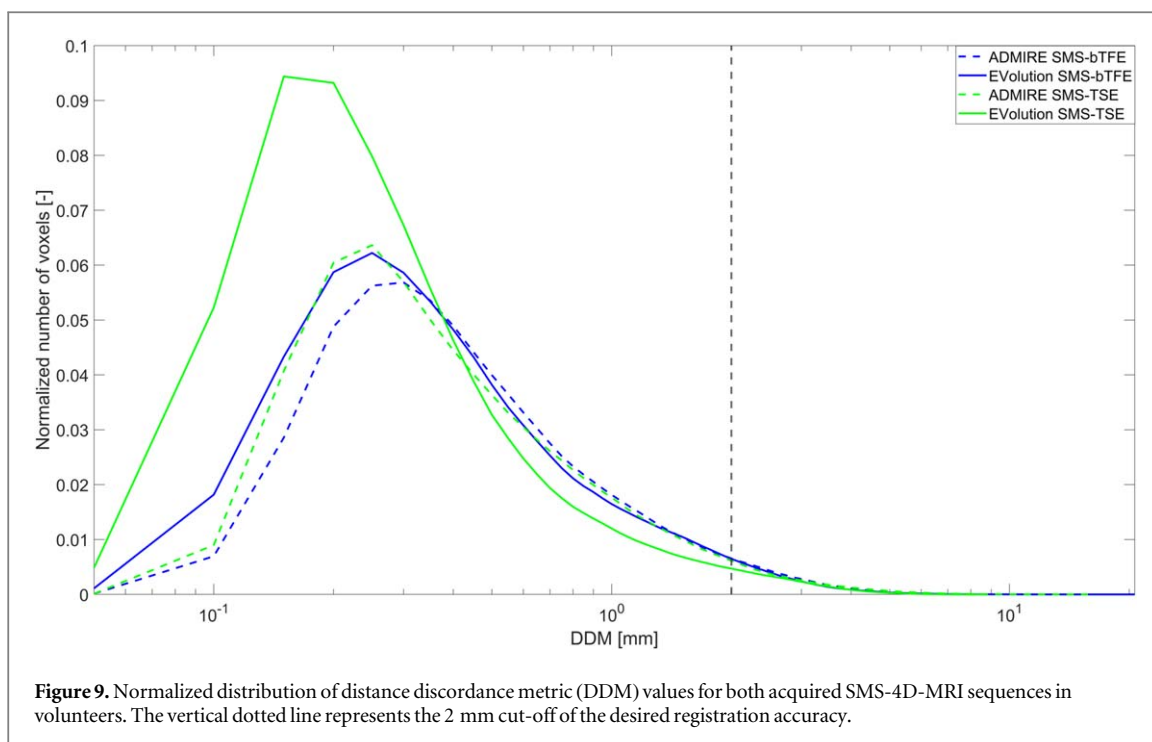


#### 4. Discussion

Two novel SMS-accelerated 4D-MRI acquisition techniques were developed and evaluated during this study, namely an SMS-bTFE and an SMS-TSE sequence. The aim was to perform data acquisition within approximately 5 min, which succeeded for both sequences. In addition, the post-processing time was intended to take less than 2 min, which has been achieved with both DIR algorithms.

For the SMS-4D-MRI acquisition, a SENSE factor of 2.5 was used to fulfill the acquisition time requirement. Effectively, this became a parallel imaging factor of 5 due to the simultaneously excitation of two slices. The Unity MR-linac has only 8 receiver channels (two 4-channel coil arrays), which resulted in less noise reduction in the SENSE reconstruction. The parallel imaging factor is limited by the number of receiver channels and noise amplification occurs when the parallel imaging factor approaches the number of receiver channels (Pruessmann *et al* 1999). A reduction of noise was found in the datasets acquired on the MR-sim, because that MRI scanner has 32 receiver channels (two 16-channel coil arrays), and therefore displayed improved reconstruction performance. Recent work has shown the development of two 16-channel (32 receiver channels total) coil arrays for the Unity MR-linac (Zijlema *et al* 2019). It is expected that this might help in the future to improve performance of the SMS-4D-MRI sequences on the Unity system, as was found for the MR-sim.

For the SMS-TSE sequence, the specific absorption rate (SAR) level was an additional limiting factor due to the length of the echo-train in the single-shot acquisition. Therefore, a refocusing angle of  $110^\circ$  was chosen that did not exceed the normal whole body SAR level ( $\leq 2 \text{ W kg}^{-1}$ ). The normal SAR level (i.e. level 0) was taken as maximum allowable SAR level during this sequence design, as this SMS-4D-MRI sequence will potentially be acquired during treatment (i.e. for 30–45 min) and should not cause patient discomfort (Grainger 2014).



Smaller refocusing angles would have decreased the scan time and the SAR level, but scans with smaller refocusing angles are more susceptible to (cardiac) motion artifacts (Madhuranthakam *et al* 2007, Litwiller *et al* 2014). In addition to the SAR limitation, the RF pulse design also introduced a limitation for data acquisition. To excite the two slices simultaneously, the two individual RF pulses were added, which resulted in a MB RF pulse

that exceeded the maximum allowed RF amplitude. As a result, the pulse lengths were scaled resulting in overlapping pulses of the excitation pulse and first refocusing pulse. To solve this problem, the echo-spacing was increased by sampling less k-space data using partial Fourier (0.64). Therefore, it is conceivable that the pulse design of the SMS-TSE sequence can be further improved by using a smaller echo spacing and therefore more k-space sampling.

The image quality acquired with the two sequences was good based on our visual assessment. The black-boundary artifact in the SMS-bTFE data occurred at water-fat interfaces due to water and fat spins that were out of phase. The SENSE artifact that appeared in all acquired volunteer datasets was observed as a small local artifact that came from the arms, which did not affect the image registration step for 23 out of 24 volunteer datasets. It is hypothesized that the more severe appearance of the SENSE artifact in the SMS-TSE acquired data was caused by limitations of the SENSE-reference scan implementation on the Unity MR-linac. The crescent-shaped SENSE artifact was only found in the image dataset of patient 1, which can be explained by the more off-center arm position compared to the other two patients.

Recent work has shown the clinical potential for a 4D-MRI driven online radiotherapy workflow (Paulson *et al* 2020). Their data acquisition was performed using a 3D sequence, providing  $T_1$  or  $T_2/T_1$  weighted images. Data acquisition took 3–3.5 min, 4D-MRI reconstruction took 6.4 min, and MidP calculation took 3.7 min on a dedicated reconstruction server for an in-plane resolution of 1.6 mm and 84 slices (interpolated from 42 acquired partitions, i.e. slices in 3D acquisition) of 2.38 mm using an in-plane FOV of  $450 \times 450 \text{ mm}^2$ . In total, it took 13.1–13.6 min to acquire the data, sort it into a 4D-MRI, and to calculate the MidP images. In contrast, in this study two 2D sequences were developed providing  $T_2/T_1$  and  $T_2$  weighted images. Data acquisition took 4.9–5.3 min, 4D-MRI binning took 0.5 min, and the MidP calculation took 1.5 or 0.8 min using ADMIRE or EVolution, respectively. In total, it took 6.2–7.3 min to acquire the data, sort it into a 4D-MRI, and to calculate the MidP images in this work. The fast acquisition and processing time of this work shows the potential to be a candidate of 4D-MRI driven online radiotherapy, as it increases patient comfort (patient shorter on table) and decreases the risk of intra-fraction baseline motion.

Previous studies on multi-slice 4D-MRI acquisitions developed either an interleaved acquisition of imaging- and navigator slices (von Siebenthal *et al* 2007), or an SMS acquisition of both slices to acquire data for the full FOV (Celicanin *et al* 2015). In both cases, the navigator slice was kept at the same spatial location for the entire scan, which lengthens the acquisition time and causes saturation/slice cross-talk effects if neighboring slices are acquired. In this study, the SMS technique of Celicanin *et al* (2015) was refined by acquiring two slices simultaneously that were half the through-plane FOV apart and both contributed to the data acquisition. This resulted in a time-efficient acquisition of the full FOV and avoided saturation effects.

A limitation of our 4D sorting approach is the empirical parameterization of some of its sub-components. For example the automatic liver-lung interface localization assumes a head-first supine patient positioning to be able to do a rough initial cropping. Moreover, the size of the search ROI was kept constant for all navigator slices and all volunteers and patients, while liver sizes vary between navigator slices and subjects. Especially the most anterior and most posterior navigator slices were challenging, as no static tissue should be present inside the search ROI to avoid template matching failure. The search ROI had to be small enough to prevent this, but had to be large enough to capture enough information about the liver-lung interface for the central navigator slices. An improvement could be to use a variable size search ROI in AP direction. For instance, it could use information from the circular Hough transform concerning the detected radii during the liver-lung interface localization.

A potential limitation of 4D-MRI sequences is that the 3D GNL corrections have to be applied to sorted data (Keesman *et al* 2019). Therefore, an in-house 3D GNL correction was developed that led to a slightly smaller in-plane FOV. This is explained by the fact that the correction was applied to the reconstructed images, and no oversampled data from outside the FOV was available that could be used in the correction at the periphery of the FOV.

The validity of the self-sorting signal is crucial for ensuring the physiological plausibility of the sorted 4D-MRI scans. Peak-to-peak (weighted SD) amplitudes were found to agree within 1.8 (1.1) mm, which is less than the voxel size, although this agreement was expected since the two signals were not truly independent. Still, this is the best validation method compared to using independent navigators. Also, the AP non-uniformity correction to normalize the self-sorting signal was found to be in excellent agreement with the correction extracted from the cine images. An additional phantom experiment confirmed the excellent agreement between extracted self-sorting signals and independent signals (see self-sorting signal: validation using a phantom setup). Even though the self-sorting signal is CC-only, we are able to resolve correlated AP and LR motion by differentiating and sorting according to inhalation and exhalation. To validate the (*in vivo*) self-sorting signal with an independent signal, an external surrogate (e.g. respiratory bellow) or an internal (e.g. 1D pencil beam) navigator signal could be acquired. However, it is known that external surrogate signals do not have to represent internal tumor and/or

OARs motion, and that internal navigators add acquisition time and can cause saturation artifacts (Stemkens *et al* 2018).

To ensure the quality of the sorted 4D-MRIs, the smoothness of the liver-lung interface in the through-plane direction was quantified for the volunteer datasets. An average RMSD range of 1.0–2.0 mm was found. Similar results were obtained by Paganelli *et al* (2015) and by van de Lindt *et al* (2018b), which both used a parabola fit on top of the liver-lung interface instead of a sagittal cine image. Volunteers 11 and 5 were found to have, on average, the worst liver-lung interface smoothness. The poor liver-lung interface smoothness can be seen in the second column in figure 8, which shows the characteristic staircase artifact in the liver-lung interface for volunteers 11 and 5. Volunteer 11 had a large peak-to-peak amplitude (36.5 mm) and a long respiratory period (8.9 s), which caused 40% of the data to be in the end-exhale phase, resulting in a lack of data in the other respiratory bins. This breathing pattern is not expected based on patient studies (Suh *et al* 2008). For volunteer 5, an irregular respiratory period (SD of 4.2 s) caused a poor liver-lung interface smoothness on average. Figure 7 showed the range of peak-to-peak amplitudes and respiratory periods involved in this study. The proposed processing method was able to sort the data for this wide range of values, indicating its robustness. Sorting performance can be improved by, for example, providing breathing instructions, as good sorting performance was found for volunteers with a regular breathing pattern. Furthermore, the scan time could be increased by acquiring more dynamics, or sorting can be started during data acquisition to predict the amount of dynamics necessary for sufficient 4D-MRI sampling.

The validity of the DVFs is crucial for ensuring the physiological plausibility of the MidP images. Although missing data of up to 26% was found in the sorted 4D-MRIs, the linear interpolation could recover image information sufficiently and did not limit the DIR for calculating the MidP images. Figure 9 showed the distribution of DDM values found for both DIR algorithms that were used. Despite the different underlying registration methods, comparable results were found for the two algorithms. From the distributions it can be seen that ADMIRE had similar performance for the two SMS sequences with different contrast, while EVolution had a larger fraction of small DDM values for the SMS-TSE data. The similar performance suggests that it is sufficient to choose the DIR algorithm that integrates best with the clinical workflow. Figure 10 showed the local regions with large DDM values that were found using EVolution. Most of them were found at locations of motion (i.e. cardiac and gastrointestinal motion) that cannot be taken into account by respiratory sorting. The figure also showed larger regions of higher DDM values for volunteers 11 and 5, compared to volunteers 1 and 8. This is in agreement with the range of RMSD values found for these volunteers. A larger RMSD means that the binned 4D-MRI suffered from artifacts. By applying registrations between the respiratory phases, this will result in larger DVFs to align the volumes to be registered and therefore a larger DDM. An average median DDM value of 0.9 mm was found within the body contour using ADMIRE by van de Lindt *et al* (2019), which is comparable to our findings for ADMIRE (median 0.7 mm), and they also found large DDM values in regions affected by cardiac and gastrointestinal motion (van de Lindt *et al* 2019). For quality assurance during a clinical workflow, the DDM map could be projected onto the MidP images to ensure the quality and reliability of the DVFs and thus the calculated MidP images.

To ensure the clinical applicability of the proposed method, patient data was included in this study from three patients with lung tumors. Previous studies by Hatabu *et al* (1999), Yamashita *et al* (1999), and Bruegel *et al* (2007) have shown good image quality and tumor visibility for their (breath-hold) single-shot sequence providing  $T_2$  weighted images for different types of lung tumors, despite the blurring artifact inherent to single-shot sequences. These findings are in agreement with the good tumor visibility found in this work using the single-shot SMS-TSE sequence. A volunteer study on the Unity MR-linac by Eccles *et al* (2019) evaluated different sequences for different anatomical sites. They found that  $T_2$  weighted images are preferred for the abdominal region and  $T_1$  weighted images for the thoracic region. However, the desired contrast might vary depending on tumor type, location, and observer. Due to the inherent contrast flexibility of 2D-based 4D-MRI, it is expected that the SMS-4D-MRI approach can be further refined for each clinical use case.

## 5. Conclusion

Two fast SMS-accelerated 4D-MRI sequences were developed resulting in  $T_2/T_1$  (bTFE) or  $T_2$  (TSE) weighted contrast, respectively. Data acquisition and processing took approximately 7 min yielding anatomically plausible 4D and 3D MidP representations with good tumor visibility. This makes SMS-4D-MRI a suitable candidate for both treatment simulation and daily MRI-guidance of thoracic and abdominal radiotherapy.

## Acknowledgments

The authors acknowledge funding by the Dutch Research Council (NWO) through project no. 17 515 (BREATHE EASY). We acknowledge research agreements with Elekta AB (Stockholm, Sweden) and Philips Healthcare (Best, The Netherlands).

## ORCID iDs

K Keijnemans  <https://orcid.org/0000-0002-9335-526X>

P T S Borman  <https://orcid.org/0000-0003-4153-2241>

J J C Verhoeff  <https://orcid.org/0000-0001-9673-0793>

M F Fast  <https://orcid.org/0000-0001-9107-4627>

## References

- Barth M, Breuer F, Koopmans P J, Norris D G and Poser B A 2016 Simultaneous multislice (sms) imaging techniques *Magn. Reson. Med.* **75** 63–81
- Borman P T S 2019 Accelerating interventional real-time MRI *PhD Thesis* Utrecht University
- Breuer F A, Blaimer M, Mueller M F, Seiberlich N, Heidemann R M, Griswold M A and Jakob P M 2006 Controlled aliasing in volumetric parallel imaging (2d caipirinha) *Magn. Reson. Med.* **55** 549–56
- Brock K K, Mutic S, McNutt T R, Li H and Kessler M L 2017 Use of image registration and fusion algorithms and techniques in radiotherapy: report of the aapm radiation therapy committee task group no. 132 *Med. Phys.* **44** e43–76
- Bruegel M, Gaa J, Woertler K, Ganter C, Waldt S, Hiller C and Rummeny E J 2007 Mri of the lung: value of different turbo spin-echo, single-shot turbo spin-echo, and 3d gradient-echo pulse sequences for the detection of pulmonary metastases *J. Magn. Reson. Imaging* **25** 73–81
- Cai J, Chang Z, Wang Z, Paul Segars W and Yin F F 2011 Four-dimensional magnetic resonance imaging (4d-mri) using image-based respiratory surrogate: a feasibility study *Med. Phys.* **38** 6384–94
- Celicanin Z, Bieri O, Preiswerk F, Cattin P, Scheffler K and Santini F 2015 Simultaneous acquisition of image and navigator slices using caipirinha for 4d mri *Magn. Reson. Med.* **73** 669–76
- de Senneville B D, Zachiu C, Ries M and Moonen C 2016 Evolution: an edge-based variational method for non-rigid multi-modal image registration *Phys. Med. Biol.* **61** 7377–96
- Eccles C L et al 2019 Magnetic resonance imaging sequence evaluation of an mr linac system; early clinical experience *Tech. Innov. Patient Support Radiat. Oncol.* **12** 56–63
- Grainger D 2014 Safety guidelines for magnetic resonance imaging equipment in clinical use *Medicines and Healthcare products Regulatory Agency* 1–86 ([https://assets.publishing.service.gov.uk/government/uploads/system/uploads/attachment\\_data/file/958486/MRI\\_guidance\\_2021-4-03c.pdf](https://assets.publishing.service.gov.uk/government/uploads/system/uploads/attachment_data/file/958486/MRI_guidance_2021-4-03c.pdf))
- Hatabu H, Gaa J, Tadamura E, Edinburgh K J, Stock K W, Garpestad E and Edelman R R 1999 Mr imaging of pulmonary parenchyma with a half-fourier single-shot turbo spin-echo (haste) sequence *Eur. J. Radiol.* **29** 152–9
- Janke A, Zhao H, Cowin G J, Galloway G J and Doddrell D M 2004 Use of spherical harmonic deconvolution methods to compensate for nonlinear gradient effects on mri images *Magn. Reson. Med.* **52** 115–22
- Keall P J et al 2006 The management of respiratory motion in radiation oncology report of aapm task group 76 *Med. Phys.* **33** 3874–900
- Keall P 2004 4-dimensional computed tomography imaging and treatment planning *Semin Radiat Oncol.* **14** 81–90
- Keesman R, van de Lindt T N, Juan-Cruz C, van den Wollenberg W, van der Bijl E, Nowee M E, Sonke J J, van der Heide U A and Fast M F 2019 Correcting geometric image distortions in slice-based 4d-mri on the mr-linac *Med. Phys.* **46** 3044–54
- Larkman D J, Hajnal J V, Herlihy A H, Coutts G A, Young I R and Ehnholm G 2001 Use of multicoil arrays for separation of signal from multiple slices simultaneously excited *J. Magn. Reson. Imaging* **13** 313–7
- Litwiller D V, Holmes J H, Saranathan M, Loening A, Glockner J, Vasanawala S and Bayram E 2014 Sensitivity of modulated refocusing flip angle single-shot fast spin echo to impulsive cardiac-like motion *Proc. of the 22th Annual Meeting of ISMRM* 1616
- Low D A et al 2003 A method for the reconstruction of four-dimensional synchronized ct scans acquired during free breathing *Med. Phys.* **30** 1254–63
- Madhuranthakam A, Busse R, Brittain J, Rofsky N and Alsop D 2007 Sensitivity of low flip angle ssfse of the abdomen to cardiac motion *Proc. of the 15th Annual Meeting of ISMRM 2007 (Berlin)* 2523
- Olsen J, Green O and Kashani R 2015 World's first applicator of mr-guidance for radiotherapy *Missouri Med.* **112** 358–60
- Paganelli C, Summers P, Bellomi M, Baroni G and Riboldi M 2015 Liver 4dmri: a retrospective image-based sorting method *Med. Phys.* **42** 4814–21
- Paganelli C et al 2018 Mri-guidance for motion management in external beam radiotherapy: current status and future challenges *Phys. Med. Biol.* **63** 22TR03
- Paulson E S, Ahunbay E, Chen X, Mickevicius N J, Chen G P, Schultz C, Erickson B, Straza M, Hall W A and Li X A 2020 4d-mri driven mr-guided online adaptive radiotherapy for abdominal stereotactic body radiation therapy on a high field mr-linac: implementation and initial clinical experience *Clin. Transl. Radiat. Oncol.* **23** 72–9
- Pruessmann K P, Weiger M, Scheidegger M B and Boesiger P 1999 Sense: sensitivity encoding for fast mri *Magn. Reson. Med.* **42** 952–62
- Raaymakers B et al 2017 First patients treated with a 1.5 t mri-linac: clinical proof of concept of a high-precision, high-field mri guided radiotherapy treatment *Phys. Med. Biol.* **62** L41–50
- Saleh Z H et al 2014 The distance discordance metric: a novel approach to quantifying spatial uncertainties in intra- and inter-patient deformable image registration *Phys. Med. Biol.* **59** 733–46
- Stemkens B, Paulson E S and Tijssen R H 2018 Nuts and bolts of 4d-mri for radiotherapy *Phys. Med. Biol.* **63** 21TR01
- Suh Y, Dieterich S, Cho B and Keall P J 2008 An analysis of thoracic and abdominal tumour motion for stereotactic body radiotherapy patients *Phys. Med. Biol.* **53** 3623–40



- van de Lindt T N, Fast M F, Van Der Heide U A and Sonke J J 2018a Retrospective self-sorted 4d-mri for the liver *Radiother. Oncol.* **127** 474–80
- van de Lindt T N, Fast M F, van Kranen S R, Nowee M E, Jansen E P, van der Heide U A and Sonke J J 2019 Mri-guided mid-position liver radiotherapy: validation of image processing and registration steps *Radiother. Oncol.* **138** 132–40
- van de Lindt T N, Sonke J J, Nowee M E, Jansen E P, van Pelt V W J, van der Heide U A and Fast M F 2018b A self-sorting coronal 4d-mri method for daily image guidance of liver lesions on an mr-linac *Int. J. Radiat. Oncol. Biol. Phys.* **102** 875–84
- van Kesteren Z, van der Horst A, Gurney-Champion O J, Bones I, Tekelenburg D, Alderliesten T, van Tienhoven G, Klaassen R, van Laarhoven H and Bel A 2019 A novel amplitude binning strategy to handle irregular breathing during 4dmri acquisition: improved imaging for radiotherapy purposes *Radiat. Oncol.* **14** 80
- von Siebenthal M, Szekeley G, Gamper U, Boesiger P, Lomax A and Cattin P 2007 4d mr imaging of respiratory organ motion and its variability *Phys. Med. Biol.* **52** 1547–64
- Wink N M, Panknin C and Solberg T D 2006 Phase versus amplitude sorting of 4d-ct data *J. Appl. Clin. Med. Phys.* **7** 77–85
- Wolthaus J W, Sonke J J, van Herk M, Belderbos J S, Rossi M M, Lebesque J V and Damen E M 2008 Comparison of different strategies to use four-dimensional computed tomography in treatment planning for lung cancer patients *Int. J. Radiat. Oncol. Biol. Phys.* **70** 1229–38
- Yamashita Y, Yokoyama T, Tomiguchi S, Takahashi M and Ando M 1999 Mr imaging of focal lung lesions: elimination of flow and motion artifact by breath-hold ecg-gated and black-blood techniques on t2-weighted turbo se and stir sequences *J. Magn. Reson. Imaging* **9** 691–8
- Yang J, Cai J, Wang H, Chang Z, Czito B G, Bashir M R and Yin F F 2014 Four-dimensional magnetic resonance imaging using axial body area as respiratory surrogate: initial patient results *Int. J. Radiat. Oncol. Bi4d-mri for radiotherapyol. Phys.* **88** 907–12
- Zijlema S E, Tijssen R H, Malkov V N, van Dijk L, Hackett S L, Kok J G, Lagendijk J J and van den Berg C A 2019 Design and feasibility of a flexible, on-body, high impedance coil receive array for a 1.5 t mr-linac *Phys. Med. Biol.* **64** 185004